Arch. Mech., 47, 2, pp. 353–377, Warszawa 1995

A gradient plasticity approach to finite element predictions of soil instability (*)

J. PAMIN (1) and R. DE BORST (2) (DELFT)

A DRUCKER-PRAGER gradient plasticity theory is applied in finite element simulation of two-dimensional localization problems in geomaterials. The gradient-dependent theory preserves well-posedness of the governing equations in presence of material instability and prevents a spurious mesh sensitivity of numerical results. An internal length scale incorporated in the theory determines the width of shear bands. Assuming weak satisfaction of the yield condition, a family of mixed finite elements is developed, in which plastic strains are interpolated with C^1-continuity in addition to the standard discretization of the displacements. Instabilities in a biaxially compressed specimen and in a slope under an increasing gravity load are simulated.

1. Introduction

FAILURE OF LOOSE and cemented granular materials like soil and rock is often accompanied by a sudden transition from a uniform deformation field into a number of localized *shear bands*. Although they are called sometimes slip planes, they have a small but finite thickness. Soil and rock specimens exhibit also a gradual degradation of stiffness with the increase of deformation and, beyond a certain level of straining, even a decrease of the load-carrying capacity called *softening*. The phenomena of *strain localization* and *softening* are closely related [1]. In simple terms, material heterogeneity induces strongly nonlinear stress-strain and volume change relations, and a local weakness of the material triggers strain localization. As a result of the inhomogeneous deformations, a softening response at the structural level is observed.

Localization can be considered as an instability in the macroscopic constitutive description of inelastic deformation [2]. Within the classical continuum theory, this kind of instability is associated with discontinuities in the strain-rate field, which, under static loading conditions, coincides with the *loss of ellipticity* of the governing partial differential equations. The acoustic tensor singularity condition [2, 3] gives the critical value of the hardening modulus, for which the bifurcation into a discontinuous strain-rate field is possible, and the direction of the discontinuity plane.

At a continuum level softening is modelled by means of a descending relation between stresses and strains (strain softening), which introduces the *material*

(*) Paper presented at 30th Polish Solid Mechanics Conference, Zakopane, September 5–9, 1994.

(1) On leave from Cracow University of Technology, Faculty of Civil Engineering.

(2) Also at Eindhoven University of Technology, Faculty of Mechanical Engineering.

instability mentioned before [4]. It has been shown that, under the assumption of small displacement gradients, the loss of material stability is a necessary condition for the loss of ellipticity [5]. Some constitutive relations for frictional materials are nonsymmetric, for instance, plasticity models do not obey the normality postulate, which may also lead to violation of material stability. In this case localization may be encountered even for a hardening model [2] and may occur prior to the limit load [6].

The loss of ellipticity may thus be induced by softening or non-associated plastic flow or a combination of the two effects. A meaningful prediction of the post-critical behaviour is impossible within the classical continuum theory, since the loss of ellipticity implies the *loss of well-posedness* of the rate boundary value problem [7]. Localization of deformation in a set of measure zero then ensues, which loses physical sense in the continuum description, since it predicts total failure without energy dissipation. As a result, numerical solutions exhibit a spurious discretization sensitivity.

The problem of mechanical representation of localized deformation can also be interpreted as follows. As long as the deformation of a soil/rock mass is almost uniform, the characteristic size of material heterogeneity is very small compared to the wave length of the deformation mode. However, the classical model fails to predict the real behaviour if the wave length of the deformation mode is comparable to the characteristic size of material heterogeneity, e.g. during localization in a shear band [8].

A natural solution is to enhance, or to *regularize*, the continuum description. There exist a few methods to regularize the governing equations [7]. They all include a so-called internal length scale that defines the width of the shear bands. In this contribution the elasto-plastic continuum description is enhanced by making the yield function dependent on the Laplacian of an equivalent strain measure [9–12]. This non-local theory is thought to reflect the micro-mechanical changes in an inhomogeneous material during failure processes. Due to the gradient dependence, the consistency condition, which governs the plastic flow, becomes a partial differential equation. To solve this equation, it is cast in a weak form and the plastic strain field is discretized in addition to the usual discretization of the displacement field.

The purpose of this paper is to examine the *gradient plasticity* approach for shear band formation in geomaterials. The assumptions of static loading and small deformations are adopted. We will limit our consideration to the non-associated Drucker–Prager model, which includes the dilatancy and non-normality of the plastic flow. In the first part of the paper we summarize the theory and the algorithm of finite element computations. In the second part, the Drucker–Prager gradient plasticity model and two special finite elements are used to solve an example of localized deformations in a plane strain sample in biaxial compression and in an embankment under an increasing gravity load.

2. Drucker–Prager gradient plasticity

Firstly, we summarize the rate boundary value problem of gradient plasticity (cf. [11, 12]). We introduce the displacement vector $\mathbf{u} = (u_x, u_y, u_z)$, the strain tensor in a vector form $\boldsymbol{\varepsilon} = (\varepsilon_{xx}, \varepsilon_{yy}, \varepsilon_{zz}, \gamma_{xy}, \gamma_{yz}, \gamma_{zx})$ and the stress tensor in a vector form $\boldsymbol{\sigma} = (\sigma_{xx}, \sigma_{yy}, \sigma_{zz}, \sigma_{xy}, \sigma_{yz}, \sigma_{zx})$. Under the assumption of small deformations and static loading we have the following equations for an elasto-plastic body occupying a volume V (Fig. 1):

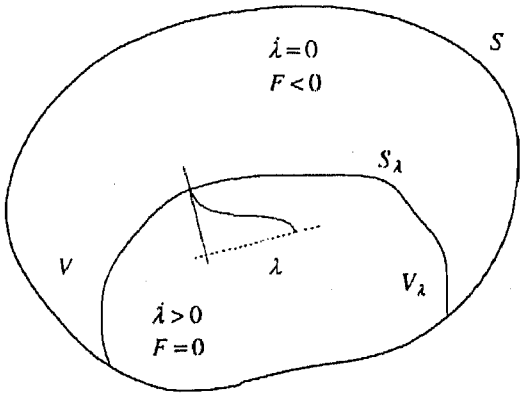

FIG. 1. Idealization of an elastic-plastic body.

$$\mathbf{L}^T \dot{\boldsymbol{\sigma}} + \dot{\mathbf{b}} = 0, \tag{2.1}$$

$$\dot{\boldsymbol{\varepsilon}} = \mathbf{L}\,\dot{\mathbf{u}}\,, \tag{2.2}$$

$$\dot{\boldsymbol{\sigma}} = \mathbf{D}^e(\dot{\boldsymbol{\varepsilon}} - \dot{\lambda}\,\mathbf{m}), \tag{2.3}$$

where superimposed dots denote the derivatives with respect to time, and the superscript T is the transpose symbol. In the above equations $\mathbf{L}$ is a differential operator matrix, $\mathbf{b}$ is a body-force vector and $\mathbf{D}^e$ is the elastic stiffness matrix. Eq. (2.3) contains the definition of the plastic strain-rate vector, called the flow rule:

$$\dot{\boldsymbol{\varepsilon}}^p = \dot{\lambda}\,\mathbf{m}, \qquad \mathbf{m} = \frac{\partial G}{\partial \boldsymbol{\sigma}}, \tag{2.4}$$

in which $\dot{\lambda}$ is a plastic multiplier and $\mathbf{m}$ defines the direction of the plastic flow. The vector $\mathbf{m}$ may be derived from a plastic potential function G.

The gradient dependence is included solely in the definition of the yield function F

$$F = F(\boldsymbol{\sigma}, \kappa, \nabla^2\kappa), \tag{2.5}$$

in which κ is an invariant plastic strain measure (the hardening parameter). Together with Eqs. (2.1)–(2.3) the Kuhn-Tucker conditions

$$\dot{\lambda} \geq 0, \qquad F \leq 0, \qquad \dot{\lambda} F = 0 \tag{2.6}$$

must be fulfilled. To complete the rate boundary value problem we specify the standard static and kinematic boundary conditions on complementary parts of the body surface S:

$$\dot{\Sigma}\, \boldsymbol{\nu}_s = \dot{\mathbf{t}}, \qquad \dot{\mathbf{u}} = \dot{\mathbf{u}}_s, \tag{2.7}$$

where $\dot{\Sigma}$ is the stress tensor in a matrix form, $\boldsymbol{\nu}_s$ denotes the outward normal to the surface S and $\mathbf{t}$ is the boundary traction vector. It is noted that with the motion equation instead of the equilibrium equation (2.1) and with additional initial conditions, an initial value problem of gradient plasticity can be formulated for dynamic loading [13].

The gradient dependence of the yield function makes the plastic consistency condition $\dot{F} = 0$ become a differential equation:

$$\left(\frac{\partial F}{\partial \boldsymbol{\sigma}}\right)^T \dot{\boldsymbol{\sigma}} + \frac{\partial F}{\partial \kappa}\dot{\kappa} + \frac{\partial F}{\partial \nabla^2 \kappa}\nabla^2 \dot{\kappa} = 0. \tag{2.8}$$

We introduce the gradient of the yield function $\mathbf{n}$:

$$\mathbf{n} = \frac{\partial F}{\partial \boldsymbol{\sigma}}, \tag{2.9}$$

the (variable) hardening modulus h:

$$h(\kappa, \nabla^2 \kappa) = -\frac{\dot{\kappa}}{\dot{\lambda}} \frac{\partial F}{\partial \kappa}, \tag{2.10}$$

and the gradient influence variable g:

$$g(\kappa) = \frac{\dot{\kappa}}{\dot{\lambda}} \frac{\partial F}{\partial \nabla^2 \kappa}, \tag{2.11}$$

which is assumed to be a function of κ only. We can now write Eq. (2.8) in the form:

$$\mathbf{n}^T \dot{\boldsymbol{\sigma}} - h\,\dot{\lambda} + g\nabla^2 \dot{\lambda} = 0. \tag{2.12}$$

For softening the modulus h is negative and the additional variable g is positive. In the simplest case h and g are constants (softening is linear). For $g = 0$ the classical flow theory of plasticity is retrieved. The consistency condition is then a

nonlinear algebraic equation, from which the plastic multiplier can be determined locally. The problem of solving Eq. (2.12), which is essentially valid in the plastic part of the body V_λ (Fig. 1), is characteristic for the present theory.

In this paper we use a finite element discretization to solve simultaneously the two coupled equations of equilibrium and plastic consistency. For this purpose we assume a weak satisfaction of the consistency condition and discretize the plastic strain field, in addition to the standard discretization of the displacements [9, 11]. This aspect will be further discussed in the remainder of the paper.

Secondly, we present the Drucker-Prager gradient plasticity model. We adopt constant values of the friction and dilatancy angles, and only the cohesion exhibits softening and gradient-dependence, which results in isotropy of the model. In the context of the *critical state* models [14], the Drucker-Prager theory is capable of describing the behaviour of geomaterials in the *supercritical* (softening) regime, but is inadequate in the *subcritical* (hardening) regime, where a cap is necessary to allow for yielding at high confining pressures. The Drucker-Prager yield function for gradient-dependent plasticity can be written as follows:

$$F = \sqrt{3J_2} + \alpha p - \beta \bar{c}_g(\kappa, \nabla^2 \kappa), \tag{2.13}$$

where J_2 is the second invariant of the deviatoric stress tensor, $p = \frac{1}{3}(\sigma_{xx} + \sigma_{yy} + \sigma_{zz})$ is the hydrostatic pressure, α and β are functions of the internal friction angle ϕ:

$$\alpha = \frac{6 \sin \phi}{3 - \sin \phi}, \qquad \beta = \frac{6 \cos \phi}{3 - \sin \phi}, \tag{2.14}$$

and $\bar{c}_g$ is a gradient-dependent measure of the cohesion. Introducing a matrix $\mathbf{P}$ and a vector $\boldsymbol{\Pi}$, defined as

$$\mathbf{P} = \begin{bmatrix} 2/3 & -1/3 & -1/3 & 0 & 0 & 0 \\ -1/3 & 2/3 & -1/3 & 0 & 0 & 0 \\ -1/3 & -1/3 & 2/3 & 0 & 0 & 0 \\ 0 & 0 & 0 & 2 & 0 & 0 \\ 0 & 0 & 0 & 0 & 2 & 0 \\ 0 & 0 & 0 & 0 & 0 & 2 \end{bmatrix}, \qquad \boldsymbol{\Pi} = \begin{bmatrix} 1/3 \\ 1/3 \\ 1/3 \\ 0 \\ 0 \\ 0 \end{bmatrix}, \tag{2.15}$$

the yield function takes the form:

$$F = \left(\frac{3}{2}\boldsymbol{\sigma}^T \mathbf{P} \boldsymbol{\sigma}\right)^{1/2} + \alpha \boldsymbol{\Pi}^T \boldsymbol{\sigma} - \beta \bar{c}_g(\kappa, \nabla^2 \kappa), \tag{2.16}$$

so that the gradient to the yield function equals

$$\mathbf{n} = \frac{3\mathbf{P}\boldsymbol{\sigma}}{2\left(\frac{3}{2}\boldsymbol{\sigma}^T \mathbf{P} \boldsymbol{\sigma}\right)^{1/2}} + \alpha \boldsymbol{\Pi}. \tag{2.17}$$

For non-associated plasticity we define the plastic potential function and its gradient in a similar fashion:

$$G = \sqrt{3J_2} + \tilde{\alpha} p, \tag{2.18}$$

$$\mathbf{m} = \frac{3\mathbf{P}\boldsymbol{\sigma}}{2\left(\frac{3}{2}\boldsymbol{\sigma}^T\mathbf{P}\boldsymbol{\sigma}\right)^{1/2}} + \tilde{\alpha}\boldsymbol{\Pi}, \tag{2.19}$$

where $\tilde{\alpha}$ is a function of the dilatancy angle ψ similar to the definition of α in Eq. (2.14). To determine the relation between $\dot{\kappa}$ to $\dot{\lambda}$ we use the strain-hardening hypothesis:

$$\dot{\kappa} = \left(\frac{2}{3}\dot{\varepsilon}^p_{ij}\,\dot{\varepsilon}^p_{ij}\right)^{1/2} = \left[\frac{2}{3}\left(\dot{\boldsymbol{\varepsilon}}^p\right)^T\mathbf{Q}\,\dot{\boldsymbol{\varepsilon}}^p\right]^{1/2}, \tag{2.20}$$

with $\mathbf{Q} = \mathrm{diag}[1,1,1,1/2,1/2,1/2]$. Substituting the plastic strain-rate vector $\dot{\boldsymbol{\varepsilon}}^p = \dot{\lambda}\,\mathbf{m}$ into Eq. (2.20) and observing that $\mathbf{PQP} = \mathbf{P}$ and $\mathbf{PQ\Pi} = \mathbf{0}$, we obtain:

$$\dot{\kappa} = \eta\,\dot{\lambda}, \qquad \eta = \left(1 + \frac{2}{9}\tilde{\alpha}^2\right)^{1/2}. \tag{2.21}$$

According to the definitions in Eqs. (2.10) and (2.11) we have:

$$h = \eta\beta\frac{\partial\bar{c}_g}{\partial\kappa}, \qquad g = -\eta\beta\frac{\partial\bar{c}_g}{\partial\nabla^2\kappa}. \tag{2.22}$$

For linear softening $\bar{c}_g$ can be written as:

$$\bar{c}_g = c_y + \frac{h}{\eta\beta}\kappa - \frac{g}{\eta\beta}\nabla^2\kappa \tag{2.23}$$

with constant h and g and with the initial value of the cohesion c_y. For nonlinear softening the cohesion changes according to:

$$\bar{c}_g = \bar{c}(\kappa) - \frac{g(\kappa)}{\eta\beta}\nabla^2\kappa, \tag{2.24}$$

and the softening modulus is calculated as:

$$h = \eta\beta\frac{\partial\bar{c}(\kappa)}{\partial\kappa} - \frac{\partial g(\kappa)}{\partial\kappa}\nabla^2\kappa. \tag{2.25}$$

The important advantage of the Drucker–Prager yield function is its smoothness, since the presence of singular edges on the yield surface poses a difficulty for the gradient plasticity algorithm [12]. In fact the Drucker–Prager yield surface also possesses a vertex at the cross-section with the hydrostatic axis. From Eq. (2.13) we calculate that at the vertex $p = \bar{c}_g\mathrm{ctg}\,\phi$. It is assumed here that the stress points in large triaxial tension, which would fall in the vertex regime $p > \bar{c}_g\mathrm{ctg}\,\phi$, are not admitted.

3. Algorithm and finite elements

An incremental formulation of the above boundary value problem gives rise to residual terms, which make a stress update necessary. The evolution of the elastic-plastic boundary within a loading step must be also considered.

In order to derive an incremental-iterative algorithm [11, 12], we require a weak satisfaction of the equilibrium condition

$$\int_V \delta \mathbf{u}^T \left(\mathbf{L}^T \boldsymbol{\sigma}_{j+1} + \mathbf{b}_{j+1} \right) dV = 0 \tag{3.1}$$

and the yield condition

$$\int_V \delta\lambda F \left(\boldsymbol{\sigma}_{j+1}, \kappa_{j+1}, \nabla^2 \kappa_{j+1} \right) dV = 0 \tag{3.2}$$

at the end of iteration $j+1$ of the current loading step, where δ denotes a variation of a quantity. Unlike in the classical plasticity algorithms, the latter condition is also satisfied in a weak sense and is only fulfilled when convergence is achieved.

Equation (3.1) can be modified using integration by parts and the standard boundary conditions $(2.7)_1$, and decomposing $\boldsymbol{\sigma}_{j+1}$ as $\boldsymbol{\sigma}_j + d\boldsymbol{\sigma}$, where d indicates an increment, i.e. the difference between the values of a variable at the end of iteration $j+1$ and iteration j:

$$\int_V \delta \boldsymbol{\varepsilon}^T \, d\boldsymbol{\sigma} \, dV = \int_V \delta \mathbf{u}^T \mathbf{b}_{j+1} \, dV + \int_S \delta \mathbf{u}^T \mathbf{t}_{j+1} \, dS - \int_V \delta \boldsymbol{\varepsilon}^T \boldsymbol{\sigma}_j \, dV. \tag{3.3}$$

Using the incremental form of the relationship between the stress and the elastic strain vector

$$d\boldsymbol{\sigma} = \mathbf{D}^e (d\boldsymbol{\varepsilon} - d\lambda \mathbf{m}), \tag{3.4}$$

we obtain the following integral equation:

$$\int_V \delta \boldsymbol{\varepsilon}^T \mathbf{D}^e (d\boldsymbol{\varepsilon} - d\lambda \mathbf{m}) \, dV = \int_V \delta \mathbf{u}^T \mathbf{b}_{j+1} \, dV + \int_S \delta \mathbf{u}^T \mathbf{t}_{j+1} \, dS - \int_V \delta \boldsymbol{\varepsilon}^T \boldsymbol{\sigma}_j \, dV. \tag{3.5}$$

We observe that this equation does not depend explicitly on the Laplacian of the plastic multiplier and has a form similar to the incremental equilibrium equations used for classical plasticity.

The yield function F in Eq. (3.2) is developed in a Taylor series around $(\boldsymbol{\sigma}_j, \kappa_j, \nabla^2 \kappa_j)$ and truncated after the linear terms:

$$F(\boldsymbol{\sigma}_{j+1}, \kappa_{j+1}, \nabla^2 \kappa_{j+1}) = F(\boldsymbol{\sigma}_j, \kappa_j, \nabla^2 \kappa_j) + \left(\frac{\partial F}{\partial \boldsymbol{\sigma}} \right)^T \Bigg|_j d\boldsymbol{\sigma} + \frac{\partial F}{\partial \kappa} \Bigg|_j d\kappa + \frac{\partial F}{\partial \nabla^2 \kappa} \Bigg|_j \nabla^2 (d\kappa), \tag{3.6}$$

where $d\kappa = \kappa_{j+1} - \kappa_j$. With the definitions (2.9)–(2.11) we obtain the following form of Eq. (3.6):

$$F(\sigma_{j+1}, \kappa_{j+1}, \nabla^2\kappa_{j+1}) = F(\sigma_j, \kappa_j, \nabla^2\kappa_j) + \mathbf{n}^T d\sigma - h\, d\lambda + g\nabla^2(d\lambda), \tag{3.7}$$

which after substitution into Eq. (3.2) gives the following integral equation:

$$\int_{V_\lambda} \delta\lambda \left[\mathbf{n}^T \mathbf{D}^e\, d\varepsilon - (h + \mathbf{n}^T \mathbf{D}^e \mathbf{m})\, d\lambda + g\nabla^2(d\lambda)\right] dV = -\int_{V_\lambda} \delta\lambda F(\sigma_j, \kappa_j, \nabla^2\kappa_j) dV. \tag{3.8}$$

The values of $\mathbf{n}$, $\mathbf{m}$, h and g on the left-hand side of Eq. (3.8) are determined at the end of iteration j, i.e. for the state defined by $(\sigma_j, \kappa_j, \nabla^2\kappa_j)$. If the same mesh is used for both the equilibrium and yield condition, i.e. if integrals over the whole volume V appear in Eqs. (3.2) and (3.8), either the admissible $\delta\lambda$ must vanish or we must enforce $F = 0$, $\mathbf{n} = \mathbf{0}$ and $d\lambda = 0$ in the elastic part of the body.

In the residual terms on the right-hand side of Eqs. (3.5) and (3.8) the stress σ_j appears. It is determined using the standard elastic predictor-plastic corrector algorithm (backward Euler type) at each integration point which is in a plastic state:

$$\sigma_j = \sigma_0 + \mathbf{D}^e \Delta\varepsilon_j - \Delta\lambda_j \mathbf{D}^e \mathbf{m}_j\,, \tag{3.9}$$

where σ_0 is the stress state at the end of the previous (converged) load increment, and Δ denotes a total increment (from state 0 to iteration j). The values of κ_j and $\nabla^2\kappa_j$ are also updated using total increments. This necessitates the use of so-called algorithmic consistent stiffness matrix $\mathbf{H}$ (instead of the elastic stiffness $\mathbf{D}^e$) in the tangent operator, otherwise the quadratic convergence rate of Newton's algorithm is not preserved [12]. Since the vector $\mathbf{m}_j$ is known only after the mapping in Eq. (3.9), it is approximated by the gradient calculated for the "trial" stress:

$$\sigma_t = \sigma_0 + \mathbf{D}^e \Delta\varepsilon_j\,. \tag{3.10}$$

To decide whether an elastic point enters the plastic regime, or whether a plastic point begins elastic unloading, the trial value of the yield function F_t is calculated at each integration point:

$$F_t = F(\sigma_t, \bar{\sigma}_g(\kappa_j, \nabla^2\kappa_j)), \tag{3.11}$$

where the gradient-dependent yield strength is determined as follows:

$$\bar{\sigma}_g = \bar{\sigma}(\kappa_j) - g(\kappa_j)\nabla^2\lambda_j\,. \tag{3.12}$$

An integration point is assumed to be in the plastic state when $F_t > 0$ and in the elastic state when $F_t < 0$. In the elastic elements $\lambda = 0$, so that for spreading of the plastic zone it is important that the numerical solution should allow for $\nabla^2\lambda > 0$ at the elastic-plastic boundary. The gradient-dependent yield strength $\bar{\sigma}_g$ is then reduced as a result of the plastic process in the neighbourhood.

In the integral equations (3.5) and (3.8) there appear at most first-order derivatives of the displacements and second-order derivatives of the plastic multiplier. Therefore, the discretization of the displacement field $\mathbf{u}$ requires C^0-continuous interpolation functions $\mathbf{N}$ and the discretization of the plastic multiplier λ requires C^1-continuous shape functions $\mathbf{h}$:

$$\mathbf{u} = \mathbf{N}\mathbf{a}, \qquad \lambda = \mathbf{h}^T\boldsymbol{\Lambda}, \tag{3.13}$$

where $\mathbf{a}$ is a nodal displacement vector and $\boldsymbol{\Lambda}$ denotes a vector of nodal degrees of freedom for the plastic multiplier field. It is noted that the left-hand side of Eq. (3.8) can be modified using integration by parts to decrease the order of the differential operator and to symmetrize the ensuing matrix operator. However, the dependence of the yield function on the Laplacian of the plastic strain measure is essential for the progressive plastification and for the determination of the non-standard residual forces on the right-hand side of Eq. (3.8), which necessitates C^1-continuous interpolation functions. To be able to use C^0-continuous shape functions, it is necessary to introduce the first derivatives of the plastic multiplier as independent, interpolated variables and add a penalty constraint to the formulation [12].

According to the linear kinematic relation (3.2), the discretization of strains has the form:

$$\boldsymbol{\varepsilon} = \mathbf{B}\mathbf{a}, \qquad \mathbf{B} = \mathbf{L}\mathbf{N}. \tag{3.14}$$

Introducing a vector $\mathbf{p}$ which contains the Laplacians of the shape functions in $\mathbf{h}$, we obtain the discretization formula for the Laplacian of the plastic multiplier:

$$\nabla^2\lambda = \mathbf{p}^T\boldsymbol{\Lambda}. \tag{3.15}$$

Substitution of the identities (3.13)–(3.15) in Eq. (3.5) gives the discretized equilibrium condition:

$$\delta\mathbf{a}^T \int_V \left[\mathbf{B}^T\mathbf{D}^e\mathbf{B}\,d\mathbf{a} - \mathbf{B}^T\mathbf{D}^e\mathbf{m}\mathbf{h}^T\,d\boldsymbol{\Lambda}\right] dV = \delta\mathbf{a}^T \int_V \mathbf{N}^T\mathbf{b}_{j+1}dV + \delta\mathbf{a}^T \int_S \mathbf{N}^T\mathbf{t}_{j+1}dS - \delta\mathbf{a}^T \int_V \mathbf{B}^T\boldsymbol{\sigma}_j\,dV. \tag{3.16}$$

Substitution of Eqs. (3.13)$_2$, (3.14) and (3.15) in Eq. (3.8) gives the discretized yield condition:

$$\delta\boldsymbol{\Lambda}^T \int_V \left[-\mathbf{h}\mathbf{n}^T\mathbf{D}^e\mathbf{B}\,d\mathbf{a} + (h + \mathbf{n}^T\mathbf{D}^e\mathbf{m})\mathbf{h}\mathbf{h}^T\,d\boldsymbol{\Lambda} - g\mathbf{h}\mathbf{p}^T\,d\boldsymbol{\Lambda}\right] dV = \delta\boldsymbol{\Lambda}^T \int_V F(\boldsymbol{\sigma}_j, \kappa_j, \nabla^2\kappa_j)\mathbf{h}\,dV. \tag{3.17}$$

Equations (3.16) and (3.17) must hold for any admissible variation of $\delta\mathbf{a}$ and $\delta\boldsymbol{\Lambda}$, so that we obtain the following set of algebraic equations [11]:

$$\begin{bmatrix} \mathbf{K}_{aa} & \mathbf{K}_{a\lambda} \\ \mathbf{K}_{\lambda a} & \mathbf{K}_{\lambda\lambda} \end{bmatrix} \begin{bmatrix} d\mathbf{a} \\ d\boldsymbol{\Lambda} \end{bmatrix} = \begin{bmatrix} \mathbf{f}_e + \mathbf{f}_a \\ \mathbf{f}_\lambda \end{bmatrix}, \tag{3.18}$$

with the elastic stiffness matrix

$$\mathbf{K}_{aa} = \int_V \mathbf{B}^T\mathbf{D}^e\mathbf{B}\,dV, \tag{3.19}$$

the off-diagonal matrices:

$$\mathbf{K}_{a\lambda} = -\int_V \mathbf{B}^T\mathbf{D}^e\mathbf{m}\mathbf{h}^T\,dV, \qquad \mathbf{K}_{\lambda a} = -\int_V \mathbf{h}\mathbf{n}^T\mathbf{D}^e\mathbf{B}\,dV, \tag{3.20}$$

the nonsymmetric gradient-dependent matrix:

$$\mathbf{K}_{\lambda\lambda} = \int_V \left[(h + \mathbf{n}^T\mathbf{D}^e\mathbf{m})\mathbf{h}\mathbf{h}^T - g\mathbf{h}\mathbf{p}^T\right] dV, \tag{3.21}$$

the external force vector and the vector of nodal forces equivalent to internal stresses:

$$\mathbf{f}_e = \int_V \mathbf{N}^T\mathbf{b}_{j+1}\,dV + \int_S \mathbf{N}^T\mathbf{t}_{j+1}\,dS, \qquad \mathbf{f}_a = -\int_V \mathbf{B}^T\boldsymbol{\sigma}_j\,dV, \tag{3.22}$$

respectively, and the vector of residual forces emerging from the weak fulfilment of the yield condition:

$$\mathbf{f}_\lambda = \int_V F(\boldsymbol{\sigma}_j, \lambda_j, \nabla^2\lambda_j)\mathbf{h}\,dV. \tag{3.23}$$

The matrix $\mathbf{K}_{\lambda\lambda}$ is nonsymmetric due to the gradient-dependence, even if the associated flow rule is considered ($\mathbf{m} = \mathbf{n}$).

Since we have a higher-order continuum formulation, the problem of additional boundary conditions for the plastic multiplier field must be addressed. The boundary conditions, derived from the variational principle for gradient plasticity [9], have the form:

$$\delta\, d\lambda = 0 \qquad \text{or} \qquad (\nabla\, d\lambda)^T \boldsymbol{\nu}_\lambda = 0. \tag{3.24}$$

For the present formulation the condition $(3.24)_2$ is automatically satisfied on the evolving elastic-plastic boundary (internal part of S_λ). However, one of the conditions (3.24) must be enforced on the surface of the body S if the tangent operator in Eq. (3.18) does not possess a sufficient rank for elastic elements.

We will consider the actual problem of a structure which is initially elastic and then, due to an inhomogeneous stress distribution, exhibits a partial plastification. If all elements are elastic, we have $\mathbf{K}_{\lambda a} = \mathbf{0}$ since the gradient vectors $\mathbf{m}$ and $\mathbf{n}$ are set to zero. Then we obtain from Eq. (3.18) the classical set of equations in $d\mathbf{a}$

$$\mathbf{K}_{aa}\, d\mathbf{a} = \mathbf{f}_e + \mathbf{f}_a \tag{3.25}$$

and the additional set of equations in $d\boldsymbol{\Lambda}$

$$\mathbf{K}^e_{\lambda\lambda}\, d\boldsymbol{\Lambda} = \mathbf{f}_\lambda\,. \tag{3.26}$$

For the elastic state we have $F < 0$ and we set the residual forces $\mathbf{f}_\lambda$ to zero. Equation (3.26) then yields the desired solution $d\boldsymbol{\Lambda} = \mathbf{0}$ if the global matrix $\widehat{\mathbf{K}}^e$ is non-singular after the element assembly and, if necessary, after the introduction of boundary conditions for the $\boldsymbol{\Lambda}$ degrees of freedom.

If plastic elements appear in the structure, we have $\mathbf{f}_\lambda \neq \mathbf{0}$ in elastic elements adjacent to the plastic zone and we compute non-zero $d\boldsymbol{\Lambda}$ from Eq. (3.26). The C^1-continuous finite elements have the feature, that these nodal values of plastic multiplier $d\boldsymbol{\Lambda}$ yield $d\lambda \approx 0$ and $\nabla^2(d\lambda) > 0$ at the integration points. As a result, the yield strength $\overline{\sigma}_g = \overline{\sigma} - g\nabla^2\lambda$ is reduced and new elastic elements can enter the plastic regime.

To avoid singularity of the tangent operator for elastic elements, the hardening modulus h in Eq. (3.21) is initially set equal to Young's modulus E. The gradient term may be neglected in the matrix $\mathbf{K}^e_{\lambda\lambda}$ for elastic elements (its inclusion only slightly influences the results). Using numerical integration the matrix $\mathbf{K}^e_{\lambda\lambda}$ is then determined as:

$$\mathbf{K}^e_{\lambda\lambda} = \sum_{ip=1}^{np} E\mathbf{h}_{ip}\mathbf{h}^T_{ip} V_{ip}\,, \tag{3.27}$$

where V_{ip} is a volume contribution of an integration point. The rank of submatrix $\mathbf{K}^e_{\lambda\lambda}$ should be examined in order to determine the number of integration points and additional boundary conditions necessary to avoid spurious zero-energy modes for the plastic multiplier field.

A high-order integration scheme and too many additional boundary conditions for the plastic multiplier field may lead to overconstrained plastic flow and may have a negative influence on the accuracy of finite element predictions. Since the yield condition may be conceived as a differential constraint to the equilibrium condition of a nonlinear solid, the number of constraints for the plastic multiplier field must be limited, otherwise the solution will be inaccurate or locked (just as it happens for some standard elements in the incompressible limit). In other words, we have a two-field theory similar to the mixed formulation with independent displacement and pressure interpolation, and a proper constraint ratio should be satisfied by the Λ degrees of freedom.

Figure 2 presents two gradient plasticity elements used in this study for plane strain configurations. Element R32EG employs quadratic serendipity interpolation of displacements, and uses bi-Hermitian shape functions for the plastic strain field and 2×2 Gauss integration. This element is the most robust of gradient plasticity elements [12] due to the special qualities of the integration stations (BARLOW points [15]), at which higher-order accuracy of the derivatives of the interpolated fields is obtained and the yield condition is satisfied exactly upon convergence. As alluded to in the preceding, the matrix $\mathbf{K}^e_{\lambda\lambda}$ requires additional constraints, which can be introduced by extra boundary conditions for derivatives of λ. For an arbitrary assembly, the conditions $\Lambda_n = 0$ and $\Lambda_{xy} = 0$ on the whole model boundary exactly supply the required number of constraints. Element T21EG has quadratic interpolation of displacements and cubic interpolation of λ, which is based on a non-conforming plate bending triangle [16]. The element has Λ_x and Λ_y degrees of freedom, but it does not fulfil the continuity requirements for λ_n on its boundary. Integration with 3 Gauss points is used, as well as 3 Hammer points at midsides of the triangle. Neither of these schemes is optimal, since return mapping to the inside of the yield locus is observed ($F_{ip} < 0$) and stress oscillations are found. Additional boundary conditions $\Lambda_n = 0$ are necessary to prevent the existence of non-zero λ modes in elastic elements.

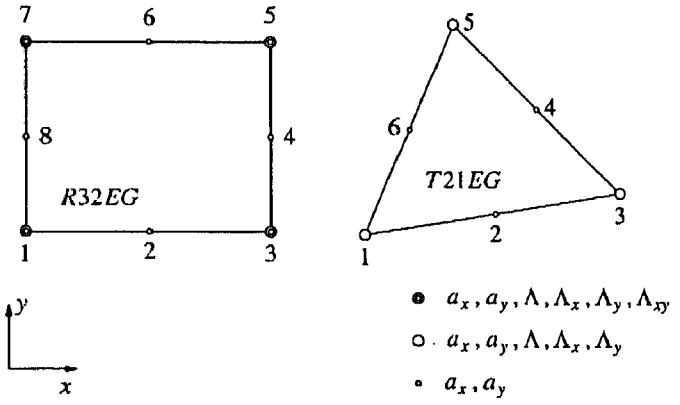

FIG. 2. Gradient plasticity elements: C^1-continuous rectangle and non-conforming triangle.

4. Applications in geomechanics

4.1. Shear layer

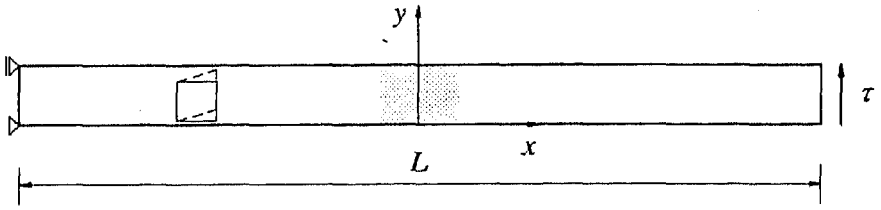

FIG. 3. Shear layer.

To illustrate the regularization introduced by the gradient-dependence we solve the one-dimensional problem of an infinite shear layer (Fig. 3). Introducing the notation $\tau = \sigma_{xy}$ and $\gamma = \varepsilon_{xy}$, the elastic constitutive relation for this case can be written as:

$$\tau = G\gamma^e, \tag{4.1}$$

where G is the shear modulus. For the plastic regime we consider the yield function of Eq. (2.13)

$$F = \sqrt{3}\tau - \beta\bar{c}_g \tag{4.2}$$

and we assume the case of volume-preserving plastic flow ($\tilde{\alpha} = 0$). Equation $(2.21)_2$ then gives $\eta = 1$ and Eq. (2.23) provides the following gradient-dependent evolution of the cohesion with a linear softening rule:

$$\bar{c}_g = c_y + \frac{h}{\beta}\kappa - \frac{g}{\beta}\frac{d^2\kappa}{dx^2}. \tag{4.3}$$

The hardening parameter can be calculated from Eq. (2.20) as:

$$\dot{\kappa} = \frac{\dot{\gamma}^p}{\sqrt{3}} \tag{4.4}$$

and both $h < 0$ and $g > 0$ are constant.

For this problem an analytical solution can be derived similar to that presented in [11] for a bar in pure tension. We solve the differential equation (4.3) rewritten as:

$$l^2\frac{d^2\kappa}{dx^2} + \kappa = \frac{\beta(\bar{c}_g - c_y)}{h}, \tag{4.5}$$

where a new parameter

$$l = \sqrt{-\frac{g}{h}}, \tag{4.6}$$

the internal length scale of our gradient-enhanced continuum, has been introduced. We notice that for Eq. (4.6) to make sense, g must be positive. Assuming a symmetric distribution of plastic strains with respect to the y-axis (Fig. 3), the solution of Eq. (4.5) is derived as:

$$\kappa = A\cos(x/l) + \frac{\beta(\bar{c}_g - c_y)}{h}. \tag{4.7}$$

We consider the evolution of the elasto-plastic process, so that Eq. (4.7) is differentiated with respect to "time":

$$\dot{\kappa} = \dot{A}\cos(x/l) + \frac{\beta\,\dot{\bar{c}}_g}{h}. \tag{4.8}$$

We assume that the plastic strains localize near the centre of the layer in a zone $(-w/2,\ w/2)$, so that w is the width of the shear band. Using the boundary condition $\dot{\kappa} = 0$ on the elastic-plastic boundary $x = \pm w/2$ we obtain

$$\dot{\kappa} = \frac{\beta\,\dot{\bar{c}}_g}{h}\left[1 - \frac{\cos(x/l)}{\cos(w/2l)}\right]. \tag{4.9}$$

The derivation has so far been general for any one-dimensional stress state. Now we return to the pure shear case and use the rate form of Eq. (4.1), the consistency condition

$$\dot{F} = \sqrt{3}\,\dot{\tau} - \beta\,\dot{\bar{c}}_g = 0, \tag{4.10}$$

Eq. (4.4) and Eq. (4.9) to determine the total shear strain rate:

$$\dot{\gamma} = \dot{\gamma}^e + \dot{\gamma}^p = \frac{\dot{\tau}}{G} + \frac{3\,\dot{\tau}}{h}\left[1 - \frac{\cos(x/l)}{\cos(w/2l)}\right]. \tag{4.11}$$

Assuming the position of the supports as in Fig. 3, we calculate the transverse velocity at the right-end of the layer $\dot{v}_r$:

$$\dot{v}_r = \int_{-L/2}^{L/2} \dot{\gamma}^e dx + \int_{-w/2}^{w/2} \dot{\gamma}^p dx = \frac{L\,\dot{\tau}}{G} + \frac{3\,\dot{\tau}}{h}[w - 2l\tan(w/2l)]. \tag{4.12}$$

The ratio of the velocity and the shear stress rate then equals

$$\frac{\dot{v}_r}{\dot{\tau}} = \frac{L}{G} + \frac{3}{h}[w - 2l\tan(w/2l)]. \tag{4.13}$$

To find the most critical equilibrium path we look for a value of w giving an aperiodic solution with the steepest descending branch. Therefore we require

$$\frac{d(\dot{\nu}_r/\dot{\tau})}{dw} = 0, \tag{4.14}$$

which results in the equation

$$\cos^2(w/2l) = 1. \tag{4.15}$$

This equation has the smallest non-trivial solution $w/2l = \pi$, so that

$$w = 2\pi l \tag{4.16}$$

with the length scale l defined by Eq. (4.6). The width of the localization zone is thus fully determined by the model parameters h and g. Substituting Eq. (4.16) into Eq. (4.13) and dividing by L gives a ratio of the average strain rate and the stress rate:

$$\frac{\dot{\nu}_r/L}{\dot{\tau}} = \frac{1}{G} + \frac{6\pi}{h}\frac{l}{L}. \tag{4.17}$$

We observe that the post-peak response is governed by the ratio l/L, which means that a size effect is incorporated in the model. The increase of the structural size L with constant l results in a more brittle behaviour.

In numerical simulations the shear layer in Fig. 3 has been discretized using 20 and 80 rectangular elements. Linear dependence relations for the relevant degrees of freedom have been added to prevent bending. The length of the layer is $L = 100\,\text{mm}$, the shear modulus $G = 10000\,\text{N/mm}^2$, Poisson's ratio $\nu = 0$, the friction angle $\phi = 0°$ ($\beta = 2.0$), the initial value of the cohesion $c_y = 1\,\text{N/mm}^2$, the softening modulus $h = -0.2G$. To trigger localization, the centre 10 mm of the layer have been assigned a 10% smaller value for c_y.

Figures 4 and 5 compare the finite element predictions for three values of the internal length: $l = 2.5$, 5 and 10 mm. The gradient influence coefficients are calculated from Eq. (4.6) as $g = 12500$, 50000 and 200000 N, respectively. The load-displacement diagrams in Fig. 4 show, that as long as all the points in the structure remain in the softening regime, the results for the two meshes with 20 and 80 elements are practically the same. The inclinations of the post-peak branches are close to the analytical values: $-\Delta\tau/\Delta\nu_r = 73.74, 26.94, 11.87\,[\text{N/mm}^3]$ for $l = 2.5$, 5 and 10 mm, respectively. When the strain in the centre elements leaves the softening branch, the load-displacement diagrams bend upwards and the localization zone broadens. This behaviour is a result of the fact that the softening modulus h goes to zero in the centre elements and g is kept constant, so that the internal length l locally increases to infinity. In this regime the calculations are stable provided the discretization used is dense enough. In Fig. 4

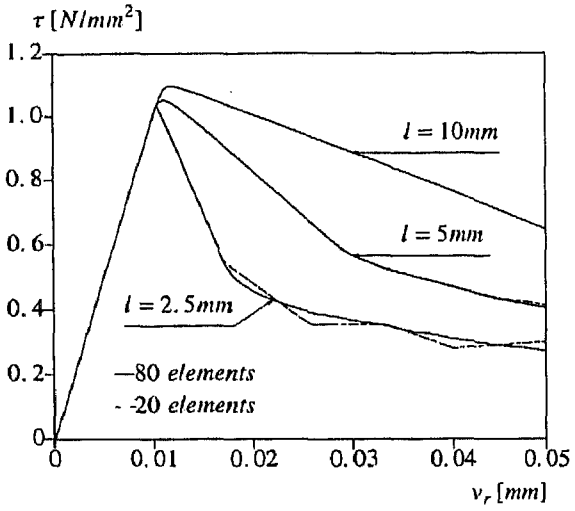

FIG. 4. Computed relations between the shear stress and the lateral displacement at the right-hand end of the shear layer.

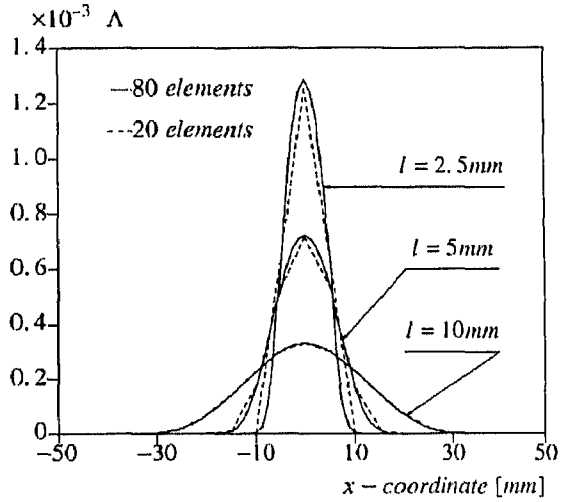

FIG. 5. Distribution of plastic multiplier along the layer for two discretizations and three values of the internal length (ν_r = 0.025mm).

the results for both meshes are similar for the larger internal length values, but for l = 2.5mm and the coarse mesh oscillations are observed. From Fig. 4 it is visible that the approach is capable of simulating the size effect, since the ratio l/L governs the response in the post-peak regime.

In Fig. 5 the distribution of nodal values of the plastic multiplier is plotted and only a slight mesh sensitivity is observed. The diagrams prove that the length parameter l determines the width of localization zone, which is close to the ana-

lytical value $w = 2\pi l$. Only for $l = 2.5\,\text{mm}$ the width of the localization zone is broader than $w = 15.7\,\text{mm}$, since for $\nu_r = 0.025\,\text{mm}$ softening has already been exhausted in the centre of the layer.

4.2. Biaxial compression

We investigate the standard plane strain biaxial compression test [17] using gradient-dependent Drucker-Prager plasticity. The test configuration has the following dimensions: $B = 60\,\text{mm}$ and $H = 120\,\text{mm}$ (Fig. 6). The bottom of the specimen is smooth and rigid, the load is applied at the top and all nodes along the upper edge are constrained to have the same vertical displacements. The material data are: elastic shear modulus $G = 1000\,\text{N/mm}^2$, Poisson's ratio $\nu = 0.2$, initial cohesion $c_y = 1\,\text{N/mm}^2$, constant softening modulus $\partial\bar{c}/\partial\kappa = -0.025G$ and friction angle $\phi = 30°$. First, we analyze the case of associated plastic flow ($\bar{\alpha} = \alpha$). According to Eq. (2.21) $\eta \approx 1.149$ and according to Eq. $(2.22)_2$, the softening modulus $h \approx -0.060G$. An internal length scale $l = 4\,\text{mm}$ is assumed and the gradient coefficient is calculated from Eq. (4.6) as $g \approx 955\,\text{N}$. Three discretizations have been used: 6×12, 12×24 and 24×48 elements R32EG.

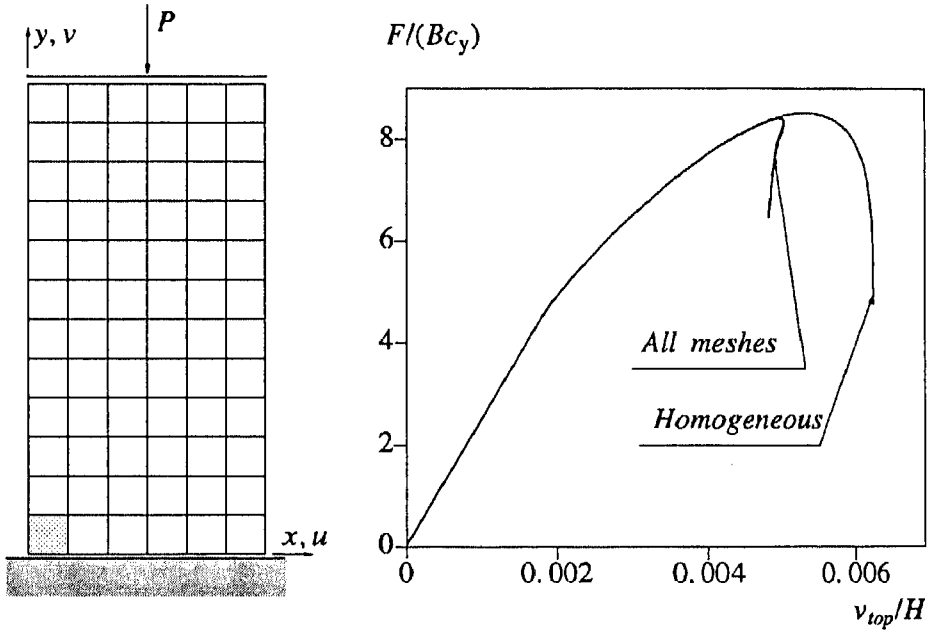

FIG. 6. Test configuration (with imperfection in the bottom left-hand corner) and load-displacement diagram for the associated plasticity case.

To follow an equilibrium path associated with the localized deformation mode, one or more slightly weaker spots (imperfections) can be introduced in the model. The bifurcation problem is then transferred into a limit problem and the imperfections initiate a localized deformation pattern. In our example an imperfect

zone with 10% smaller c_y is introduced in the bottom left-hand corner (Fig. 6). Calculations are performed under arc-length control.

Figure 6 presents the relative load versus relative displacement diagrams for the case of homogeneous deformations, which is obtained without inserting imperfections, and for the gradient plasticity model (all meshes). The pressure-dependence of the yield function causes an initial stress build-up and hardening behaviour, despite the cohesion softening. The whole specimen shows an almost uniform plastic flow and a shear band-type localization is impossible at the onset of plastification. This behaviour agrees with the fact that for this stress state the acoustic tensor singularity condition [2, 3] gives a critical value of the softening modulus, which is much smaller than the value used in our calculations.

At a load level $F/(Bc_y) \approx 8.4$ a bulging localization mode emerges as shown in Fig. 7. The results obtained for the gradient-dependent continuum using the three meshes are almost identical also in the post-critical regime.

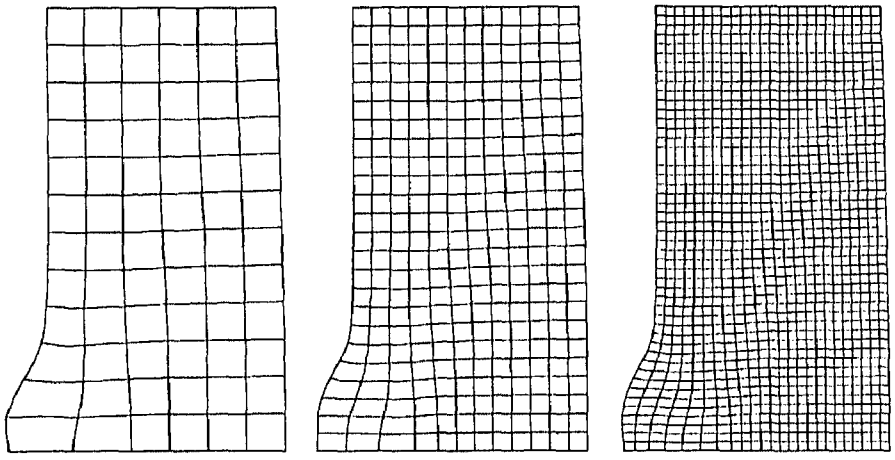

FIG. 7. Incremental deformations of the gradient-dependent model at $F/(Bc_y) = 7.3$.

During the plastic process the relations between the stress components change and the critical value of the softening modulus increases. While at the onset of instability the analytical expression from [3] gives $h_{cr} \approx -0.13G$, which is smaller than the input data, so that shear-band formation is impossible, in the post-critical regime the bulging mode promotes a shear-band mode (Fig. 8).

Next, we consider the non-associated plasticity case. The test data are the same as before with the exception of the dilatancy angle ψ, which is now equal to zero (volume preserving plastic flow). The value the softening modulus is $h \approx -0.052G$ and the gradient constant is $g \approx 831\,\mathrm{N}$. Calculations are now performed under displacement control.

The load-displacement curves for the three discretizations are shown in Fig. 9, under homogeneous and inhomogeneous deformations. In this figure the shear band obtained for classical, gradient-independent plasticity ($l = 0$) has also been

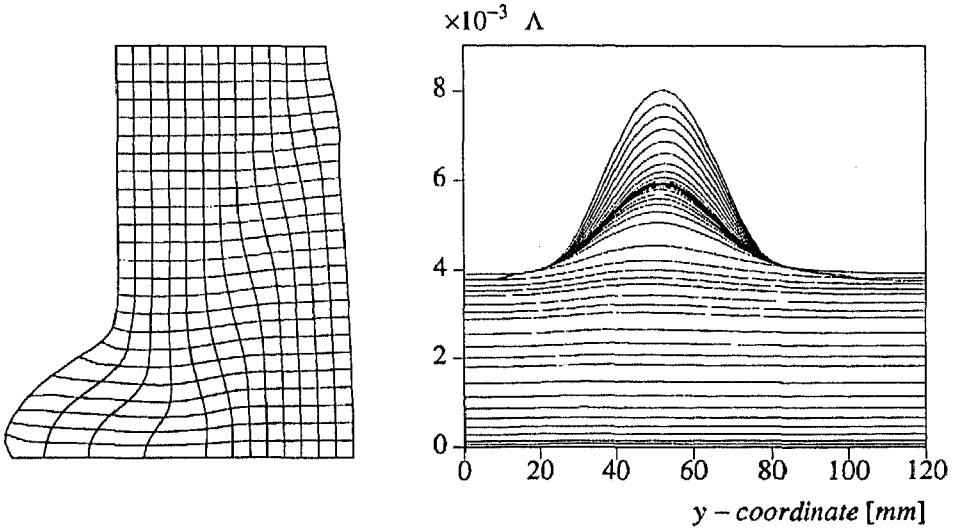

FIG. 8. Emergence of a shear band in presence of the bulging mode. Incremental displacements of the medium mesh at $F/(Bc_y) = 6.4$ (left) and the evolution of the plastic multiplier distribution along the vertical symmetry axis (right).

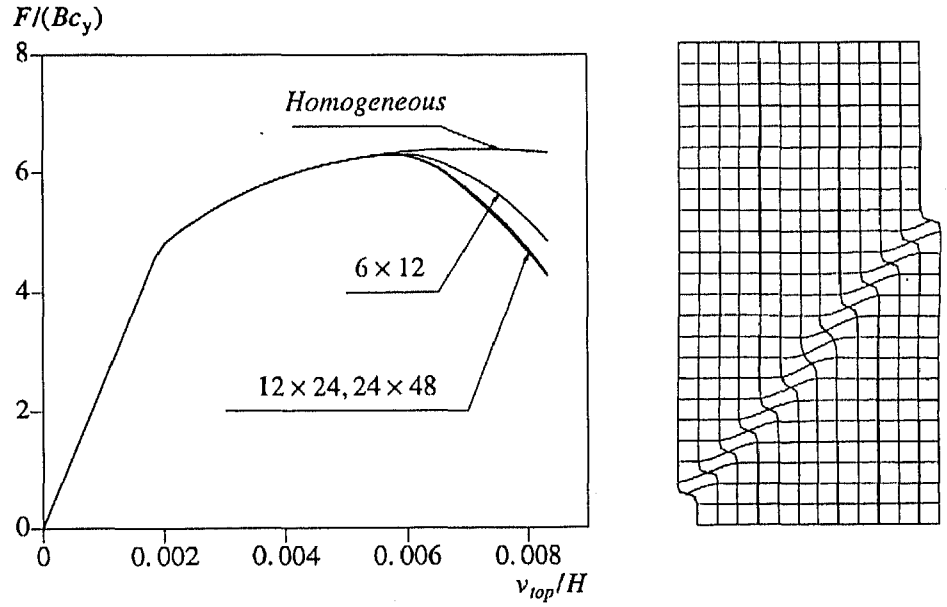

FIG. 9. Load-displacement diagram for the non-associated plasticity case and the incremental deformations of the gradient-independent model for the medium mesh.

plotted. It shows how in the classical continuum the gradient-independent finite elements attempt to predict localization in a discrete plane. The shear band width converges to the smallest value admitted by the discretization. For other meshes

completely different solutions are computed in the post-critical regime. On the other hand, the gradient-dependent model removes the spurious mesh sensitivity. Although the response for the coarse mesh is a bit too stiff, it is almost the same for the medium and fine mesh. The shear band width is practically the same for all meshes (Fig. 10). Even though we now analyze a biaxial stress state, the relation $w = 2\pi l$, derived for the one-dimensional case in the previous section, gives a good approximation of the shear band width.

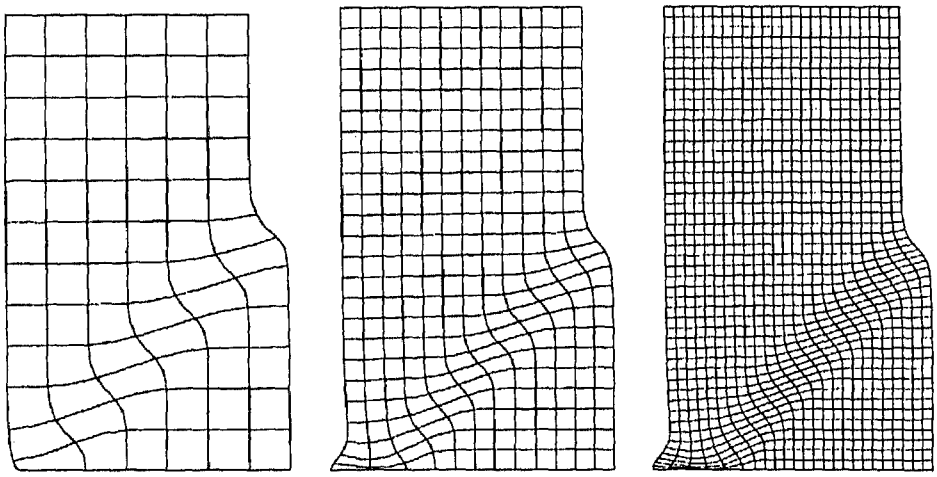

FIG. 10. Incremental deformations of the gradient-dependent model at $v_{top}/H = 0.0083$.

The non-associated plasticity model results in a more ductile and less stable behaviour than the associated model. At the onset of plastification localization is impossible ($h_{cr} \approx -0.427G$ according to [3]), but at the onset of numerically predicted shear banding the analytical value of the critical hardening modulus is already positive ($h_{cr} \approx 0.03G$ according to [3]).

4.3. Slope stability

Figure 11 shows two configurations used for the analysis of soil mass stability under an increasing gravity load. On the left we present a slope with an inclination of 45° (cf. [18]), and on the right a vertical embankment. In both cases the lower edge is fixed and the right edge is supported in the horizontal direction.

The material data are based on [18]: Young's modulus $E = 2 \cdot 10^8\,\mathrm{N/m^2}$, Poisson's ratio $\nu = 0.25$, initial cohesion $c_y = 2000\,\mathrm{N/m^2}$, friction angle $\phi = 20°$, dilatancy angle $\psi = 10°$. The soil density $\rho = 1000\,\mathrm{kg/m^3}$ is adopted. The linear softening rate for cohesion is $\partial\bar{c}/\partial\kappa = -0.01G$. The strain hardening hypothesis gives $\eta = \dot{\kappa} / \dot{\lambda} \approx 1.015$ and the softening modulus $h \approx -0.060G$. The results for two internal length scales $l = 0.02\,\mathrm{m}$ and $l = 0.04\,\mathrm{m}$ are compared (the gradient constants are $g \approx 688\,\mathrm{N}$ and $g \approx 2752\,\mathrm{N}$, respectively).

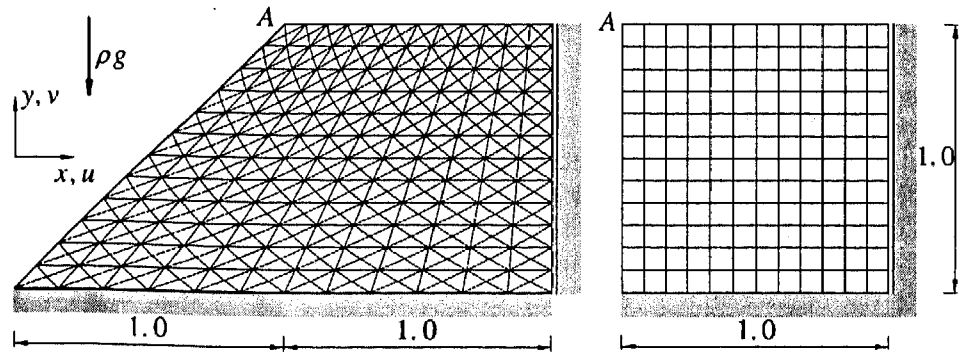

FIG. 11. Inclined and vertical embankment models (dimensions in m).

For the first configuration we use two crossed-diagonal meshes with $12 \times 12 \times 4$ and $24 \times 24 \times 4$ six-noded triangles T21EG with 3 integration points. For the second configuration we use three discretizations with 12×12, 24×24 and 48×48 eight-noded elements R32EG with a 2×2 integration scheme. The calculations are performed under the arc-length or single displacement control. In the latter case the vertical displacement of point A is the controlling parameter (cf. Fig. 11).

We begin the discussion with the vertical embankment. Figure 12 presents the calculated relations between the gravity load factor and the vertical displacement of point A obtained using the Drucker-Prager gradient plasticity model. When the gravity load reaches the level 0.6, the first plastic points occur in the bottom left-hand corner of the embankment. A shear band then gradually extends towards the upper edge and a softening response follows.

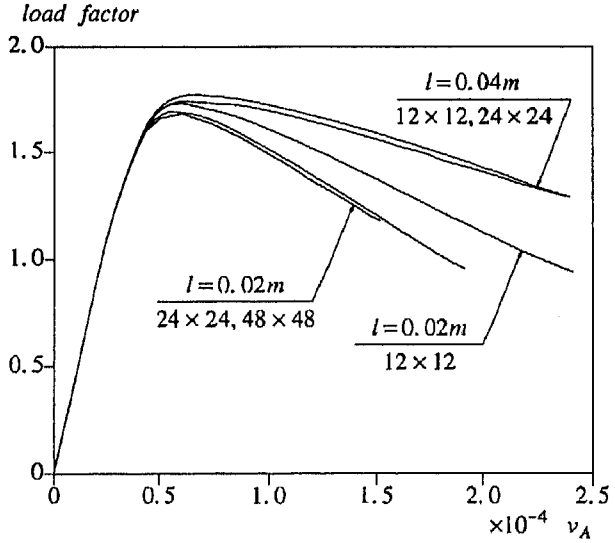

FIG. 12. Mesh sensitivity of load-displacement diagrams for the vertical embankment and gradient plasticity elements R32EG.

Figure 13 presents the incremental displacements at the final load level for the smaller internal length $l = 0.02$m. It is observed that the medium and fine mesh produce almost identical results. A too stiff response is found in Fig. 12 for the coarse mesh (12×12 elements). The shear band width defined by the assumed internal length is close to the smallest possible size that can be reproduced by this mesh. Therefore the representation is insufficient, while for the larger internal length $l = 0.04$m the coarse and medium meshes give already similar results. Figure 14 illustrates the dependence of the shear band width w on the assumed value of the internal length l. As for the biaxial compression test, a good correspondence is found with the analytical relation $w = 2\pi l$ derived for the pure shear case.

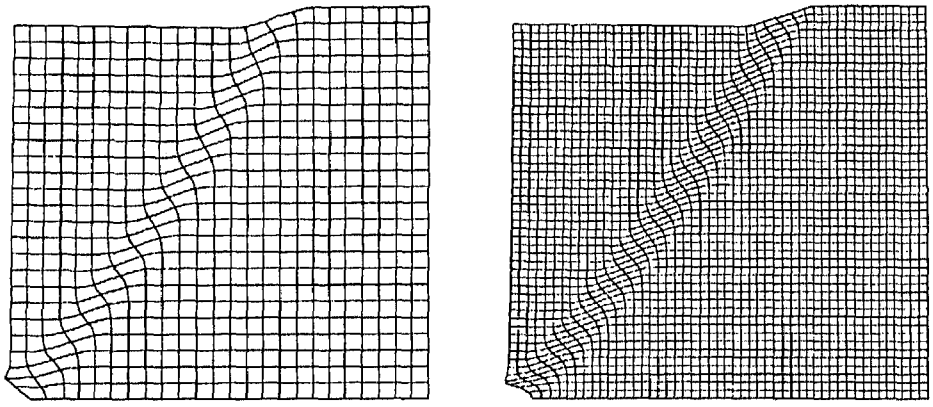

FIG. 13. Incremental deformation patterns for the medium and fine mesh ($l = 0.02$m).

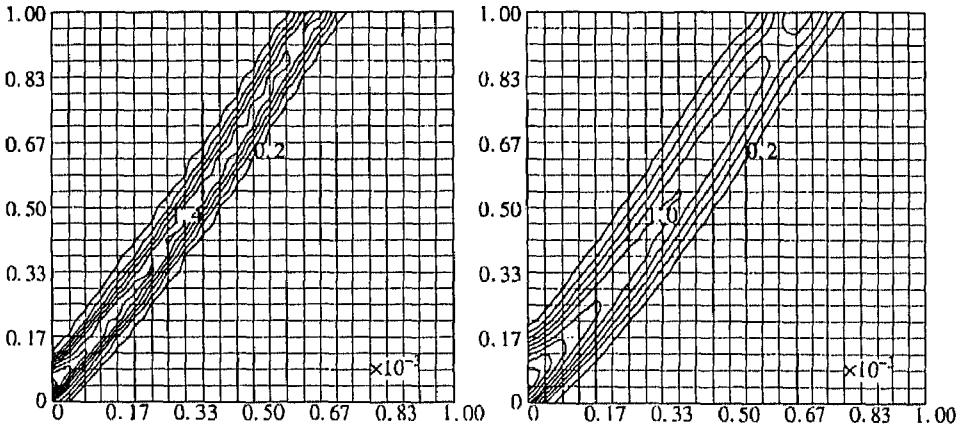

FIG. 14. Contour plots of equivalent plastic strain for $l = 0.02$m (left) and $l = 0.04$m (right).

Next, we analyze the stability of the slope in Fig. 11. In the gradient plasticity calculations the length scale $l = 0.04$m is used. Figure 15 presents the load-displacement diagrams. With the increase of the dead-weight (at the load

factor value 1.8), the compressed soil mass starts to plastify at the bottom of the embankment. The plastic zone then gradually expands upwards and at the peak-load a shear band forms, along which a part of the soil mass slides down.

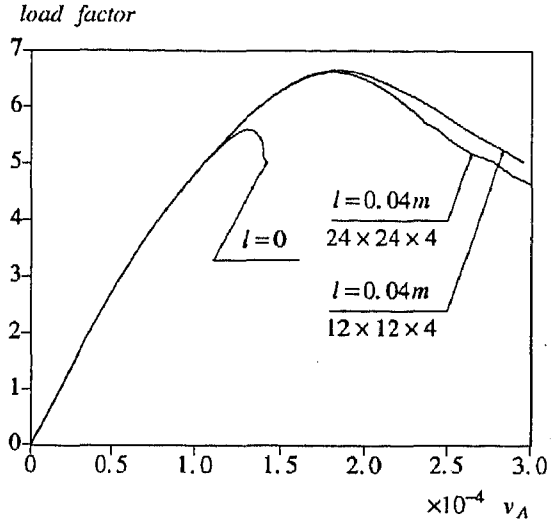

FIG. 15. Classical versus gradient plasticity solutions for the slope stability problem in terms of gravity load factor and vertical displacement at point A.

Calculations for classical softening plasticity case ($l = 0$) fail soon after the formation of the shear band. The gradient plasticity algorithm gives a more stable behaviour. The peak-load is higher and the response is more ductile when the gradient terms are included. The results for both analyzed meshes are close, but not the same (Fig. 15).

Figure 16 presents the final incremental deformations for the gradient plasticity case and $24 \times 24 \times 4$ element mesh. The expected smoothing effect is observed and the curved shear band has the width of several elements. Figure 17 compares

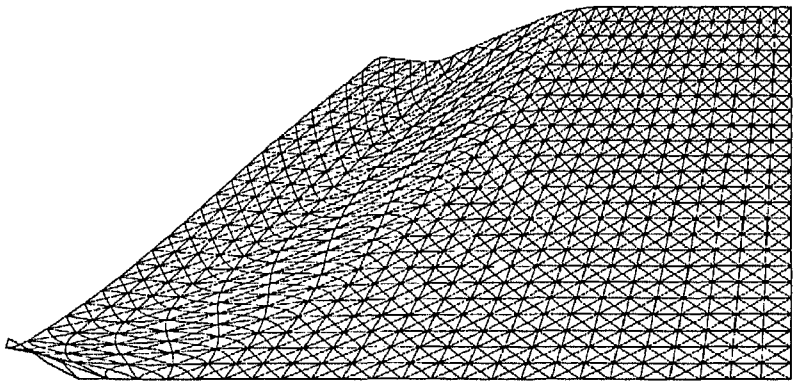

FIG. 16. Incremental deformation pattern for the finest mesh ($24 \times 24 \times 4$ elements T21EG) and $l = 0.04$ m.

the contour plots of the equivalent plastic strain obtained for the two analyzed discretizations. The strains are slightly more localized for the fine mesh, but the shear band width $w \approx 0.25\,\mathrm{m}$ is well reproduced.

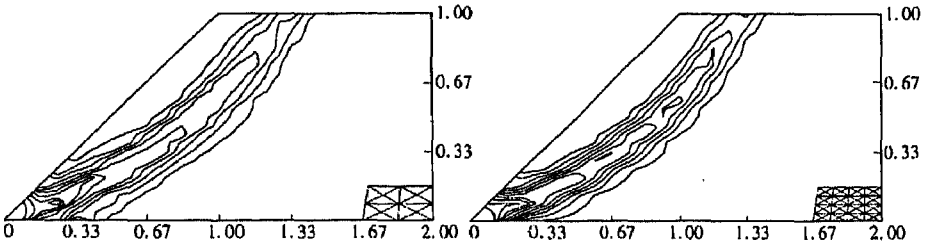

FIG. 17. Contour plots of equivalent plastic strain for two discretizations ($l = 0.04\,\mathrm{m}$).

1. Conclusions

The employed gradient plasticity theory, which incorporates a yield function dependent on higher-order spatial derivatives of a plastic strain measure, preserves ellipticity of the governing equations in the post-critical regime. Therefore, the boundary value problem for a softening continuum remains well-posed. An internal length scale is present in the theory and determines the width of the shear localization bands. Therefore, the results of finite element simulations are almost insensitive to the mesh refinement.

The fundamental feature of the used algorithm is a weak (and not pointwise) satisfaction of the yield condition, which is coupled with a weak equilibrium condition. The dependence of the yield function on the Laplacian of the plastic strain measure induces the necessity of C^1-continuous interpolation of the plastic strain field in the incremental formulation. A C^1-continuous rectangular element and a non-conforming triangular element have been implemented and applied in some soil instability problems.

The results have shown that the gradient plasticity models may be successfully applied in the numerical simulation of localization phenomena in frictional materials. The Drucker–Prager flow theory with a gradient-dependent softening cohesion is an example of a plasticity formulation that can be employed for prediction of various instability modes in overconsolidated soils. A further investigation of advanced elasto-plastic models like the Cam-clay model [14] with the gradient localization limiter is necessary. The experimental determination of the internal length scale for various geomaterials is also of primary importance.

2. Acknowledgements

The calculations have been carried out with the DIANA finite element code of TNO Building and Construction Research. The financial support of the Commis-

sion of the European Communities through the Brite-Euram program (project BE-3275) is gratefully acknowledged.

References

1. H.E. READ and G.A. HEGEMIER, *Strain softening of rock, soil and concrete. A review article*, Mech. Mater., **3**, 271–294, 1984.
2. J.W. RUDNICKI and J.R. RICE, *Conditions for the localization of deformation in pressure-sensitive dilatant materials*, J. Mech. Phys. Solids, **23**, 371–394, 1975.
3. K. RUNESSON, N.S. OTTOSEN and D. PERIĆ, *Discontinuous bifurcations of elastic-plastic solutions at plane stress and plane strain*, Int. J. Plasticity, **7**, 99–121, 1991.
4. G. MAIER and T. HUECKEL, *Nonassociated and coupled flow rules of elastoplasticity for rock-like materials*, Int. J. Rock Mech. Min. Sci. & Geomech. Abstr., **16**, 77–92, 1979.
5. K.J. WILLAM and G. ETSE, *Failure assessment of the extended Leon model for plain concrete*, [in:] Proc. Second Int. Conf. Computer Aided Analysis and Design of Concrete Structures, N. BIĆANIĆ *et al.* [Eds.], Pineridge Press, Swansea, 851–870, 1990.
6. P.A. VERMEER and R. DE BORST, *Non-associated plasticity for soils, concrete and rock*, Heron, **29**, 3, 1984.
7. R. DE BORST, L.J. SLUYS, H.-B. MÜHLHAUS and J. PAMIN, *Fundamental issues in finite element analyses of localization of deformation*, Engng. Comput., **10**, 99–121, 1993.
8. H.-B. MÜHLHAUS, R. DE BORST and E.C. AIFANTIS, *Constitutive models and numerical analyses for inelastic materials with microstructure*, [in:] Proc. Seventh Conf. Int. Assoc. Comp. Methods and Advances in Geomechanics, G. BEER *et al.* [Eds.], Balkema, Rotterdam, 377–385, 1991.
9. H.-B. MÜHLHAUS and E.C. AIFANTIS, *A variational principle for gradient plasticity*, Int. J. Solids Structures, **28**, 845–857, 1991.
10. I. VARDOULAKIS and E.C. AIFANTIS, *A gradient flow theory of plasticity for granular materials*, Acta Mech., **87**, 197–217, 1991.
11. R. DE BORST and H.-B. MÜHLHAUS, *Gradient-dependent plasticity: Formulation and algorithmic aspects*, Int. J. Num. Meth. Engng., **35**, 521–539, 1992.
12. J. PAMIN, *Gradient-dependent plasticity in numerical simulation of localization phenomena*, Dissertation, Delft University of Technology, Delft 1994.
13. L.J. SLUYS, R. DE BORST and H.-B. MÜHLHAUS, *Wave propagation, localization and dispersion in a gradient -dependent medium*, Int. J. Solids Structures, **30**, 1153–1171, 1993.
14. A. GENS and D.M. POTTS, *Critical state models in computational geomechanics*, Engng. Comput., **5**, 178–197, 1988.
15. J. BARLOW, *Optimal stress locations in finite element model*, Int. J. Num. Meth. Engng., **10**, 243–251, 1976.
16. O.C. ZIENKIEWICZ and R.L. TAYLOR, *The finite element method*, fourth edition, Vol. 2, Chapter 1, McGraw-Hill, London 1991.
17. R. DE BORST, *Numerical methods for bifurcation analysis in geomechanics*, Ing.-Arch., **59**, 160–174, 1989.
18. M. ORTIZ, Y. LEROY and A. NEEDLEMAN, *A finite element method for localized failure analysis*, Comp. Meth. Appl. Mech. Engng., **61**, 189–214, 1987.

DELFT UNIVERSITY OF TECHNOLOGY,
FACULTY OF CIVIL ENGINEERING, DELFT, THE NETHERLANDS.

Received September 14, 1994.